1
2   **Revision 1**

3   **Compressibility of synthetic Mg-Al tourmalines to 60 GPa**

4   Eleanor J. Berryman[1*], Dongzhou Zhang[2], Bernd Wunder[3], Thomas S. Duffy[1]

5   [1]Department of Geosciences, Princeton University, Princeton, NJ 08544, USA

6   [2]Hawai'i Institute of Geophysics and Planetology, University of Hawai'i at Manoa, Honolulu, HI

7   96822, USA

8   [3]Chemistry and Physics of Earth Materials, GFZ German Research Centre for Geosciences,

9   14473 Potsdam, Germany

10   *berryman.eleanor@gmail.com

11

12   **Abstract**

13   High-pressure single-crystal X-ray diffraction patterns on five synthetic Mg-Al tourmaline of

14   near end-member composition (dravite $NaMg_3Al_6Si_6O_{18}(BO_3)_3(OH)_3OH$, K-dravite

15     $KMg_3Al_6Si_6O_{18}(BO_3)_3(OH)_3OH$, magnesio-foitite • $(Mg_2Al)Al_6Si_6O_{18}(BO_3)_3(OH)_3OH$, oxy-

16   uvite $CaMg_3Al_6Si_6O_{18}(BO_3)_3(OH)_3O$, and olenite $NaAl_3Al_6Si_6O_{18}(BO_3)_3O_3OH$, where •

17   represents an *X*-site vacancy) were collected to 60 GPa at 300 K using a diamond-anvil cell and

18   synchrotron radiation. No phase transitions were observed for any of the investigated

19   compositions. The refined unit-cell parameters were used to constrain 3rd-order Birch-

20   Murnaghan pressure-volume equation of states with the following isothermal bulk moduli (K_0 in

21   GPa) and corresponding pressure derivatives ($K_0' = \partial K_0/\partial P)_T$: dravite K_0=97(6), K_0'=5.0(5); K-

22   dravite K_0=109(4), K_0'= 4.3(2); oxy-uvite K_0=110(2), K_0'=4.1(1); magnesio-foitite K_0=116(2),

23   K_0'=3.5(1); olenite K_0=116(6), K_0'=4.7(4). Each tourmaline has highly anisotropic behavior

24   under compression, with the **c** axis 2.8 - 3.6 times more compressible than the **a** axis at ambient

25   conditions. This anisotropy decreases strongly with increasing pressure and the **c** axis is only

26   ~14% more compressible than the **a** axis near 60 GPa. The octahedral *Y-* and *Z*-sites'

27   composition exerts a primary control on tourmaline's compressibility, whereby Al content is

28   correlated with a decrease in the **c**-axis compressibility and a corresponding increase in K_0 and

29   K_0'. Contrary to expectations, the identity of the *X*-site-occupying ion (Na, K, or Ca) does not

30   have a demonstrable effect on tourmaline's compression curve. The presence of a fully vacant *X*

31   site in magnesio-foitite results in a decrease of K_0' relative to the alkali and Ca tourmalines. The

32   decrease in K_0' for magnesio-foitite is accounted for by an increase in compressibility along the

33   **a** axis at high pressure, reflecting increased compression of tourmaline's ring structure in the

34   presence of a vacant *X* site. This study highlights the utility of synthetic crystals in untangling the

35   effect of composition on tourmaline's compression behavior.

36

37   **Keywords**   Tourmaline, synthetic, single-crystal X-ray diffraction, equation of state,

38   diamond-anvil cell

39

40   **Introduction**

41   Tourmaline is the most common borosilicate and is found in a variety of rock-forming

42   environments throughout the crust (van Hinsberg et al. 2011). This supergroup mineral

43   comprises at least 33 end-member species represented by the general structural formula

44    $XY_3Z_6T_6O_{18}(BO_3)_3V_3W$. Tourmaline's complex crystal chemistry allows its structure to

45   incorporate at least 26 elements of varying size and charge (Bosi, 2018). Of these, the current

46   end-member-defining site-occupants are Na, Ca, K, and vacancy (•) at the nine-fold-coordinated

47   *X* site; Mg, Fe^{2+}, Fe^{3+}, Al, Li, Mn, Cr, V at the octahedral *Y* and *Z* sites; Si and Al at the

48   tetrahedral *T* site; OH and O at the *V* site; and OH, O and F at the *W* site. The B site is the only

49   cation site that does not exhibit solid solution. However, B is not limited to the B site. In both

50   natural and synthetic Al-rich tourmalines, significant amounts of excess B (<2.3 pfu) have been

51   reported to occur at the *T* site (e.g., Tagg et al. 1999; Schreyer et al. 2000, 2002; Marler et al.

52   2002; Hughes et al. 2000, 2001; Marschall et al. 2004; Ertl et al. 2012a; Kutzschbach et al.

53   2016).

54

55   Tourmaline's stability throughout the crust and possibly the uppermost mantle is surprising in

56   view of the expectation that the presence of multiple coordination environments in its structure

57   might limit tourmaline's stability (Bosi, 2018). At ambient pressure, tourmaline has been

58   experimentally shown to be stable from 150 K until it dehydrates at 1200 – 1280 K and is then

59   reported to break down to products including cordierite at 1400 K (Hemingway et al., 1996).

60   Upon compression, single-crystal X-ray diffraction (XRD) up to 23.6 GPa supported by

61   luminescence spectroscopy suggests dravitic tourmaline undergoes a subtle second-order phase

62   transition from rhombohedral *R*3*m* to *R*3 symmetry at 15 GPa (O'Bannon et al., 2018).

63   Luminescence spectroscopy at higher pressure shows the latter structure remains (meta)stable to

64   at least ~65 GPa (O'Bannon et al., 2018). Dravitic tourmaline has been synthesized up to 6-8

65   GPa, <1000°C, above which it decomposes to a number of Mg-Al phases (Krosse, 1995). The

66   upper limit of tourmaline's stability is reduced in a Si-saturated system and Mg-Al tourmaline

67   has been shown experimentally to decompose around 4.5 - 5 GPa and 700°C (Ota et al., 2008).

68

69   Tourmaline's complex chemistry and crystal properties historically distinguished it as a mineral

70   of scientific interest (Dutrow and Henry, 2011). The occurrence of striking concentric and sector

71   zoning within single crystals results from the low intra-volume diffusion of elements in its

72   structure even at high temperature (Henry and Dutrow, 1996). Combined with its resistance to

73   mechanical and chemical weathering, tourmaline's compositional zoning underlies its traditional

74   application as a sediment provenance indicator (e.g., Henry and Dutrow, 1992). More recently,

75   efforts are being made to decode tourmaline's record of its host rock's evolution through

76   pressure, temperature, and compositional space. To fully unlock tourmaline's potential as a

77   petrogenetic indicator mineral (e.g., Henry and Guidotti, 1985; van Hinsberg et al, 2011), an

78   understanding of its end-member thermodynamic parameters and crystal chemistry at high

79   pressure and temperature is needed.

80

81   Current knowledge of the elastic properties of tourmaline is limited to a few ultrasonic elasticity

82   studies on natural samples at ambient conditions (Helme and King, 1978; Tatli and Özkan, 1987;

83   Pandey and Schreuer, 2012) and high-pressure powder and single-crystal XRD (up to 27.8 GPa

84   Li et al., 2004; 18 GPa Xu et al., 2016, 23.6 GPa O'Bannon et al., 2018). The reported ambient

85   isothermal bulk moduli (K_0) and their pressure derivatives ($K_0' = (\partial K_0/\partial P)_T$) show considerable

86   scatter (**Table 1**), which has been proposed to reflect compositional variability of the

87   investigated samples (Helme and King, 1978). Composition, especially Al content, is known to

88   strongly influence tourmaline's long-range crystal structure through variation of its unit-cell

89   parameters (Bosi et al. 2010). It is therefore likely that composition may influence tourmaline's

90   other properties, such as its behavior under compression. The Fe content of tourmaline has been

91   correlated with variations in some of the single-crystal elastic constants, however the

92   investigated compositional range and corresponding elastic variability were limited (Pandy and

93   Schreuer 2012). Similar to other cyclosilicates, such as beryl and cordierite, tourmaline is known

94   to have strongly anisotropic compressibility, whereby the **c** axis perpendicular to the ring

95   structure is more compressible than the **a** axis. Due to the size and location of the highly

96   compressible *X* site directly above the ring structure in the **c** direction (**Fig. 1**), it has been

97   hypothesized that the *X* site may exert a primary control on tourmaline's compressibility,

98   especially along **c** (e.g., Xu et al., 2012; O'Bannon et al., 2018).

99

100   Synthetic crystals provide an optimal means to explore the relative effects of pressure,

101   temperature, and fluid composition on the incorporation of elements in tourmaline (von Goerne

102   et al., 2011; Berryman et al., 2014, 2015, 2016a; Kutzschbach et al., 2017). Moreover, the

103   characterization of synthetic crystals has provided valuable insight into tourmaline's chemical

104   flexibility and how composition affects tourmaline's long- and short-range crystal structure (Ertl

105   et al. 2003; London et al. 2006; Wunder et al. 2015; Berryman et al., 2016b; Setkova et al. 2009,

106   2017). Whereas natural tourmaline crystals represent complex solid solutions of multiple end-

107   members and contain significant amounts of minor elements, synthetic crystals can be grown

108   with restricted compositions, allowing for more direct determination of the chemical control on

109   physical properties.

110

111   High-pressure XRD experiments on minerals constrain their stability and their pressure-volume

112   equation of state (P-V EoS). Moreover, studies on minerals of varying composition provide

113   valuable information on the effect of chemistry on these mineral properties (e.g., Zhang 1998,

114   Zhang et al. 1999; Ballaran et al., 2012; Xu et al., 2019). Here, a collection of synthetic Mg-Al

115   tourmaline (dravite, K-dravite, magnesio-foitite, oxy-uvite, and olenite) is used to constrain the

116   300-K P-V EoS of five tourmalines with distinct *X*-site occupancies (Na, K, Ca, and vacancies)

117   and Mg-Al contents to 60 GPa.

118

119   **Experimental methods**

120   *Synthetic samples*

121   The magnesio-foitite and oxy-uvite samples were synthesized by Berryman et al. (2016b) and the

122   olenite sample by Kutzschbach et al. (2016). Information on the synthesis and characterization

123   (electron microprobe analysis EMPA, powder and single-crystal X-ray diffraction XRD and

124   Raman spectroscopy) is available in Berryman et al. (2016b) for magnesio-foitite (sample MF2)

125   and oxy-uvite (sample CN11) and in Kutzschbach et al. (2016) for olenite (columnar crystals;

126   MK1). The dravite (sample 471-1) and K-dravite (sample 471-2) were newly synthesized for this

127   study using a method modified after Berryman et al. (2015). Information on the synthesis and

128   characterization (EMPA, powder and single-crystal XRD) is available in the Supplementary

129   Material.

130

131   The five synthetic samples investigated in this study represent four distinct Mg-Al tourmaline

132   species (dravite, K-dravite, oxy-uvite, magnesio-foitite) and the Na-Al tourmaline species,

133   olenite. The compositions of the general cation sites (*X*, *Y*, *Z*, and *T*) for each of the synthetic

134   tourmaline samples are in **Table 2**. The theoretical end-member species represented by this

135   collection have the following idealized formulae [$XY_3Z_6T_6O_{18}(BO_3)_3V_3W$]: dravite

136    $NaMg_3Al_6Si_6O_{18}(BO_3)_3(OH)_3OH$, K-dravite $KMg_3Al_6Si_6O_{18}(BO_3)_3(OH)_3OH$, oxy-uvite

137    $CaMg_3Al_6Si_6O_{18}(BO_3)_3(OH)_3O$, magnesio-foitite • $(Mg_2Al)Al_6Si_6O_{18}(BO_3)_3(OH)_3OH$, and

138   olenite $NaAl_3Al_6Si_6O_{18}(BO_3)_3O_3OH$. The *X*-site compositions of the Mg-Al tourmalines are

139   distinct, representing each of the principal *X*-site-occupying ions of the tourmaline supergroup:

140   Na, Ca, vacancy • , and K. Although K most commonly occurs in minor or trace amounts in

141   tourmaline, K-dominant species have been found (e.g., Grice et al. 1993; Shimizu and

142   Ogasawara 2005). There is currently only one K-bearing tourmaline species recognized by the

143   International Mineralogical Association's Commission on New Minerals, Nomenclature, and

144   Classification (IMA-CNMNC): maruyamaite $K(MgAl_2)(Al_5Mg)Si_6O_{18}(BO_3)_3(OH)_3O$ (Lussier et

145   al., 2016).

146

147   The olenite sample is distinguished from the other samples by the absence of Mg at the *Y* and *Z*

148   sites, which are instead fully occupied by Al. It is important to note that the idealized ordering of

149   Mg and Al between the *Y* and *Z* sites present in the theoretical end-member formulae of the Mg-

150   Al tourmalines is never observed in natural or synthetic tourmaline. The large difference in

151   average <*Y*-O> and <*Z*-O> bond lengths imposed by such ordering would destabilize

152   tourmaline's structure (Bosi and Lucchesi, 2007; Bosi, 2018). The Mg-Al tourmalines

153   investigated here therefore show significant Mg-Al disorder between the *Y* and *Z* sites. Likely

154   owing to their high Al content, the synthetic magnesio-foitite and olenite contain significant

155   amounts of tetrahedral B: 0.34(4) and 1.4(1) ^{T}B pfu, respectively (**Table 2**). In addition, all the

156   synthetic tourmalines have a significant number of *X*-site vacancies. As a result of their variable

157   short- and long-range crystal structure, the investigated tourmalines span a range of unit-cell

158   volumes observed for natural tourmalines (**Fig. 2**).

159

160   *X-ray diffraction*

161   The high-pressure single-crystal XRD patterns were collected using symmetric diamond-anvil

162   cells (DAC) equipped with type 1a diamonds with 300-μm culets mounted on X-ray transparent

163   cBN (upstream) and WC (downstream) seats. A sample chamber was made in a Re gasket

164   indented to a ~30-40 μm thickness using either an electric-discharge machining drill (154-μm

165   hole diameter) or a laser drilling system (200-μm hole diameter). An individual tourmaline

166   crystal (~14×14×80 μm or smaller) was loaded together with a ruby sphere and a piece of

167   powdered gold as pressure standards in each DAC. A neon-gas pressure-transmitting medium

168   was loaded using a gas-loading system (Rivers et al., 2008). High-pressure single-crystal X-ray

169   diffraction patterns were collected up to 60 GPa in <5 GPa pressure steps along with ambient X-

170   ray diffraction patterns at beamline 13BM-C at the GeoSoilEnviroCARS (GSECARS) sector of

171   the Advanced Photon Source. The synchrotron X-ray was monochromated to a wavelength of

172   λ=0.434 Å (28.6 keV) within a 1 eV bandwidth. The X-ray spot was focused to ~12 (horizontal)

173   ×18 (vertical) μm on the sample and diffraction images were collected on a MAR165 CCD area

174   detector. The sample-detector distance (~155 mm) and detector tilt were calibrated using a NIST

175   LaB_6 standard. Angle-dispersive X-ray diffraction data for tourmaline was collected in 1° steps

176   (step scans) across each DAC's downstream opening angle (dravite 27°, K-dravite 37°, oxy-uvite

177   40°, magnesio-foitite 33°, and olenite 27°). Exposures (10-20 s/°) were collected with the detector

178   in line with the incident X-ray ($2\theta = 0°$). In addition, wide-step exposures across each half of the

179   DAC opening angle were collected with the detector at $2\theta = 0°$ and with the detector rotated 10°

180   around the 2θ axis. A wide scan of X-ray diffraction data from the tourmaline crystal and the

181   powdered gold pressure standard across the entire downstream opening angle of the DAC at one

182   detector position ($2\theta = 0°$) was also collected at each pressure step.

183

184   The diffraction quality of the different crystals varied as indicated by the number of sharp single-

185   crystal diffraction spots that were indexed to hexagonal symmetry: oxy-uvite, 142 peaks;

186   magnesio-foitite, 78 peaks; olenite, 68 peaks; dravite, 55 peaks; and K-dravite, 38 peaks.

187   Diffraction spots from each step-scan diffraction pattern were identified and combined using the

188   GSE_ADA/RSV software package (Dera et al., 2013). The unit cell and orientation matrices

189   were identified with the program CELL_NOW (Bruker AXS Inc.). Refinement of the unit-cell

190   parameters was done using peaks identified in the combined wide-scan diffraction patterns

191   collected at two detector positions.

192

193   Gold's powder XRD pattern was integrated using Dioptas (Clemens and Prakapenka, 2015) and

194   the unit-cell parameter determined from the position of the (111) diffraction peak. Pressure was

195   determined using the pressure-volume equation of state of Dewaele et al. (2004) and Fei et al.

196   (2007). The neon pressure medium crystallizes at 4.7 GPa (Finger et al., 1981), leading to

197   reduced hydrostatic conditions inside the DAC. The differential stress at each pressure point was

198   estimated using the approach of (Singh and Kenichi, 2001), which relies on comparing gold's

199   unit-cell parameter based on the (002), (022), and (111) diffraction peaks and the elastic

200   anisotropy factor of Tsuchiya and Kawamura (2002). In all experiments, detectable differential

201   stress appeared at ~10 GPa and increased with pressure, but never exceeded 0.6 GPa.

202

203   **Results and Discussion**

204

205   *X-ray diffraction*

206   The unit-cell parameters of the tourmalines at each pressure step are listed in **Table 3** and

207   presented in **Fig. 3**. The unit-cell parameters were consistently refined to a rhombohedral cell at

208   all investigated pressure points and no phase transformations were identified over the

209   investigated pressure range. O'Bannon et al. (2018) reported a subtle phase transition in dravitic

210   tourmaline at 15 GPa resulting from a change in the distortion behavior of the ring structure

211   under compression. This phase transition changes the space group from $R3m$ to $R3$, reflecting the

212   loss of the mirror plane. This second-order phase transition does not change the topology of the

213   tourmaline structure and rhombohedral symmetry was maintained. It would not be detectable in

214   our datasets because it is not associated with a change in unit-cell volume.

215

216   The pressure -- unit-cell volume (P-V) dataset for each investigated tourmaline was fit to both

217   2nd and 3rd order Birch-Murnaghan P-V equations of state (P-V EoS) using fully weighted

218   parameters and the EosFit-7c program (Angel et al. 2014; Gonzalez-Platas et al. 2016). The

219   resulting ambient isothermal bulk moduli (K_0) and their respective pressure derivatives (K_0') are

220   shown in **Table 1**. The values are in reasonable agreement with previous studies. The ambient

221   unit-cell volume (V_0) constrained by the fit for each composition is in close agreement with

222   those determined for single crystals from the corresponding synthesis experiment: dravite

223   1556.4(4) $Å^3$; K-dravite 1569.2(3) $Å^3$; oxy-uvite 1570.7(3) $Å^3$; magnesio-foitite 1562.1(4) $Å^3$;

224   olenite 1491.3(2) $Å^3$. The quality of the fits can be further evaluated by considering the fit of the

225   P-V EoS in normalized pressure vs Eulerian strain space (F_E-f plots in Supplementary Material).

226   In these coordinates, the 3rd order Birch-Murnaghan P-V EoS is needed to fit the data of all

227   tourmaline compositions, with the exception of synthetic dravite, where the 2nd order Birch-

228   Murnaghan P-V EoS fits the data equally well.

229

230   A parametrized version of the 3rd-order Birch Murnaghan EoS was fit to the weighted axial unit-

231   cell parameters (a and c) as a function of pressure using the EosFit-7c program. The resulting

232   axial moduli (M_{a0} and M_{c0}) were converted to linear compressibilities at ambient conditions (β_{a0}

233   and β_{c0}) following the approach of Angel et al. (2014) (**Table 4**). The linear compressibility at

234   each pressure step was calculated following the approach of Xia et al. (1998) (**Fig. 4**). The

235   results confirm tourmaline's highly anisotropic elasticity, whereby the **c** axis is 2.8-3.6 times

236   more compressible than the **a** axis at ambient conditions, consistent with previous findings (see

237   references in **Table 1**). This behavior is similar to other cyclosilicates (e.g., beryl; Hazen et al.

238   1986) and is interpreted to reflect the relative incompressibility of the ring structures parallel to **a**

239   (**Fig. 1**). The presence of the highly compressible X site in the **c** direction further contributes to

240   tourmaline's anisotropic elasticity (O'Bannon et al. 2018). Tourmaline's elastic anisotropy

241   decreases with increasing pressure and the axial compressibilities converge near 60 GPa at which

242   point the **c** axis is only ~14% more compressible than the **a** axis (**Fig. 4**).

243

244   **Influence of tourmaline composition on compressibility**

245

246   *Primary role of Al content*

247   Al is a key cation in tourmaline, as indicated by it being a defining constituent of 28 out of the 33

248   end-member species. Consequently, it is a major element in all naturally occurring tourmaline

249   samples. Al is primarily incorporated at the octahedral sites (Y and Z), with preference for the

250   network-forming Z site (Bosi, 2018). To a lesser extent, it is also incorporated at the T site

251   (**Table 2**).

252   The Al content of tourmaline is known to exert a strong influence on the long-range crystal

253   structure, particularly in terms of a negative correlation between Al content and the c unit-cell

254   parameter (Bosi et al., 2010). Interestingly, the Z site composition is more strongly correlated to

255   unit-cell volume than the larger X site (**Fig. 2**). This likely reflects the importance of the long-

256   range network formed by the coordinated Z sites in both the **a** and **c** directions. Moreover, the

257   formation of 3_1 spiral chains of Z coordination polyhedra along **c** accounts for Al's strong

258   influence on the length of the **c** axis (**Fig. 1**). In addition, high Al contents have been correlated

259   to increased incorporation of tetrahedral B (^{T}B) in tourmaline (Ertl et al., 2008a). As a result, ^{T}B

260   has been observed in natural olenite (e.g., 1 ^{T}B pfu; Hughes et al., 2000) and is present in

261   significant quantities in the synthetic olenite investigated here (**Table 2**). Incorporation of B at

262   the T site reduces the average $<T$-O$>$ bond length and corresponding the unit-cell volume (**Fig.**

263   **2;** Ertl et al. 2018), albeit not as significantly as the octahedral sites. By encouraging the

264   incorporation of ^{T}B, Al content strengthens its own influence on the unit-cell volume of

265   tourmaline.

266

267   Here, the Mg-free synthetic olenite has both octahedral sites fully occupied by Al, allowing the

268   direct investigation of the effect of Al on tourmaline compressibility compared with Mg-Al

269   tourmalines. The small size of Al relative to other octahedral-site-occupying ions results in

270   synthetic olenite having the smallest Y and Z sites of all the investigated synthetic tourmaline, as

271   well as being smaller than naturally occurring tourmalines (**Fig. 2**). As expected, the high Al

272   content leads to a significant reduction in the unit-cell parameters at all pressures relative to the

273   Mg-Al tourmalines (**Fig. 3**).

274

275 In regards to tourmaline's bulk compressibility, there is no immediately obvious correlation with

276 Al content. The ambient isothermal bulk modulus of olenite is comparable to that of Mg-bearing

277 magnesio-foitite and its pressure derivative to those of the dravitic tourmalines (**Table 1**).

278 However, when comparing K_0 and K_0' values, it is important to bear in mind that these

279 parameters covary during fitting (Bass et al. 1981; Angel 2000). When the covariance is

280 considered, it becomes evident that the bulk compressibility of the Mg-Al tourmaline (dravite,

281 K-dravite, oxy-uvite, and magnesio-foitite) are correlated, with olenite showing distinctly higher

282 K_0 and K_0' values (**Fig. 5**).

283

284 The lower bulk compressibility of Al-dominant tourmaline is primarily accounted for by its

285 reduced compressibility along the **c**-axis. There is a correlation between the c_0 unit-cell

286 parameter and the ambient linear compressibility of the **c** axis (β_{c0}) (**Fig. 6**). As the c_0 parameter

287 is sensitive to the Al content of tourmaline, especially at the Z site, olenite, followed by the most

288 Al-rich of the Mg-Al tourmaline, magnesio-foitite, are the least compressible in the **c**-axis

289 direction. In contrast, no correlation between a_0 and β_{a0} is observed. The influence of the Al

290 content on tourmaline's compressibility especially along **c** is interpreted to reflect the primary

291 control of the 3_1 ZO_6 spiral chains, preferentially occupied by Al. The correlation between linear

292 compressibility along **c** (β_c) and Al content does not persist at high pressure. Instead, β_c values

293 for the different tourmaline compositions converge by 30 GPa.

294

295 *Secondary role of X-site-occupancy*

296 The nine-fold-coordinated X site is the largest site in the tourmaline structure and is located

297 directly above the center of the six-membered ring along **c** (**Fig. 1**). Similar to the role of large

298   cations and water in other ring silicates, the X site has been posited to be responsible for

299   tourmaline's relatively increased compressibility in the **c** direction (Dietrich 1985). Tourmaline

300   exhibits distinctly increased compressibility along **c** in comparison to the cyclosilicates beryl and

301   cordierite, which has been thought to reflect the higher concentration of the highly compressible

302   X site in tourmaline (Xu et al. 2016; O'Bannon et al. 2018). The occupancy and composition of

303   the X site has therefore been previously expected to have a significant influence on tourmaline

304   compressibility.

305

306   The Mg-Al tourmalines investigated here (K-dravite, dravite, oxy-uvite, and magnesio-foitite)

307   each have a distinct X-site composition, including all the major X-site occupants of the

308   tourmaline group (K, Na, Ca, and • , respectively). Contrary to expectations, the X site does not

309   exert a primary control on tourmaline compressibility, as K_0 is similar for all the tourmalines.

310   However, the presence of a nearly completely vacant X site in magnesio-foitite is correlated with

311   a lower K_0' value relative to the other tourmalines (**Fig. 5**). It should be noted that in the 3rd order

312   P-V EoS, dravite's P-V behavior is fit with a high K_0' value. This may be taken to reflect its low

313   number of X-site vacancies. However, this interpretation is not supported by the K_0' value of K-

314   dravite, which has a similar number of X-site vacancies (**Table 2**). As shown in the F_E-f plots in

315   the Supplementary Material, the 2nd order P-V EoS fits the dravite data equally well. As a result,

316   we have chosen not to interpret the high K_0' value of dravite's 3rd order P-V EoS as reflecting a

317   compositional control.

318

319   Close inspection of the linear compressibility at high pressure (**Fig. 4**) suggests that the lower

320   K_0' value of magnesio-foitite results from increased compressibility along **a** (β_a) at high pressure.

321   Compression along **a** is expected to be influenced by compression of the six-membered ring,

322   which lies parallel to **a**. Although the *T* site has relatively low compressibility, deformation of

323   the six-membered ring it forms plays a central role in tourmaline's behavior under compression

324   (O'Bannon et al. 2018). More specifically, in natural dravite, O'Bannon et al. (2018) show this

325   deformation comprises a continuous increase in ditrigonality of the ring structure combined with

326   crimping and puckering up to ~15 GPa. After the loss of the mirror plane above ~15 GPa, ring

327   deformation was reported to be primarily accommodated by increasing ditrigonality and

328   tetrahedral rotation. Interestingly, it is near this pressure that magnesio-foitite begins displaying

329   increased compressibility along **a** relative to the principally *X*-site-occupied tourmalines.

330   Magnesio-foitite is known to have a distinct ring morphology characterized by increased

331   crimping, a feature that also affects its electronic structure (Berryman et al. 2016). It is therefore

332   not surprising that magnesio-foitite might exhibit slight differences in the compressive behavior

333   of its ring structure. We can therefore speculate that the presence of a vacant *X* site is somehow

334   facilitating increased compression along **a** relative to the other Mg-Al tourmalines. However, it

335   is important to note that olenite maintains reduced compressibility along **a** despite having

336   significant *X*-site vacancies. This observation underlines the predominant role of Al content and

337   the octahedral sites on the structure's compressibility in all directions.

338

339   **Implications**

340   The tourmaline supergroup is exceptional in terms of its chemical flexibility. The presence of

341   three-, four-, six-, and nine-fold coordinated sites in its structure allow it to incorporate a range

342   of cations of varying size and charge. This apparent divergence from Pauling's rule of parsimony

343   might be expected to reduce tourmaline's stability (Bosi 2018). Despite this, tourmaline is

344   observed to be stable throughout the crust (van Hinsberg et al. 2011) and potentially in the

345   uppermost mantle (Marschall et al. 2008). Under static compression at room temperature, none

346   of the five investigated synthetic tourmalines show any indication of a reconstructive phase

347   transition or amorphization up to 60 GPa, revealing the remarkable metastability of this complex

348   structure. However, the possibility of an undetected subtle phase transition cannot be ruled out as

349   O'Bannon et al. (2018) reported a second-order phase transition in dravitic tourmaline from

350   rhombohedral $R3m$ to rhombohedral $R3$ at ~15.4 GPa. Tourmaline maintains its topology

351   through this transition and the high-pressure phase differs from the lower-pressure structure only

352   by the absence of the mirror plane.

353

354   Tourmaline's metastability to high pressure exists in sharp contrast to the behavior of other

355   cyclosilicates. Cordierite undergoes two reconstructive first-order phase transitions characterized

356   by increasing amounts of polymerization of Si by 15.4 GPa at room temperature (Finkelstein et

357   al. 2015). Beryl, another cyclosilicate of interest, is observed to be stable to at least 9.5 GPa in

358   high-pressure XRD experiments (Fan et al. 2015), but *ab initio* calculations and high-pressure

359   spectroscopic data indicate a displacive phase transition is expected at 14 GPa (Prencipe et al.

360   2011; O'Bannon and Williams 2016). These cyclosilicates differ from tourmaline by the

361   presence of open channels formed by the alignment of the six-membered rings within their long-

362   range structure. In contrast, the polar six-membered rings in tourmaline are separated by the

363   presence of three corner-sharing Y-site octahedra as well as the nine-fold-coordinated X site.

364   Tourmaline's structure is additionally differentiated from other cyclosilicates by its framework

365   of Z-site octahedra that extend in the **a** and **c** directions. It is important to note that X-site-vacant

366   magnesio-foitite exhibited the same level of metastability at the X-site-occupied tourmalines.

367   Moreover, magnesio-foitite exhibits generally similar compressibility, including anisotropic

368   compressibility, as the other tourmalines. This comparison not only indicates that the *X*-site-

369   occupying ion does not have a strong influence on tourmaline's compressibility, but that it is also

370   not pivotal in the stability of the tourmaline structure. Our results instead forward the hypothesis

371   that the chemically flexible octahedral *Y* and *Z* sites are primarily responsible for the mechanical

372   flexibility and extensive (meta)stability of the tourmaline structure.

373

374   Tourmaline's extensive chemical flexibility and high-pressure, room-temperature behavior is

375   therefore perhaps more comparable to that of the clinopyroxenes and amphiboles than it is to the

376   cyclosilicates. Grunerite amphibole is metastable to at least 25 GPa (Yong et al. 2018) and

377   clinopyroxene does not exhibit a reconstructive phase transition until 50 GPa (Plonka et al.,

378   2012). Moreover, the two displacive phase transitions recorded in clinopyroxenes and

379   amphiboles are due to the kinking of the chains of tetrahedra (Welch et al., 2007; Yong et al.,

380   2018). This behavior is interestingly analogous to the behavior of tourmaline's six-membered

381   ring under compression. During compression, the ring structure in dravite is reported by

382   O'Bannon et al. (2018) to exhibit increasing ditrigonality and puckering.

383

384   Synthetic crystals provide critical insight into the role of composition on tourmaline's properties.

385   They are especially useful for characterizing the effect of end-member components that are

386   common, but rarely dominant in natural tourmaline, such magnesio-foitite and olenite. Questions

387   concerning the effect of particular components on tourmaline's properties in tourmaline can thus

388   unambiguously be explored without having to survey a wide range of chemically complex

389   natural tourmaline compositions. Here, comparison of the Mg-Al tourmalines (dravite, K-dravite,

390   magnesio-foitite, and oxy-uvite) to a pure Al-tourmaline (olenite) revealed the primary role of Al

391   on tourmaline's compressibility. In addition, comparison of a completely *X*-site-vacant

392   tourmaline (magnesio-foitite) to the nominally *X*-site-occupied tourmalines revealed the

393   secondary role of *X*-site-occupancy on compressibility along **a**. Substitution of Na, Ca, and K did

394   not have a demonstrable effect on compressibility. Moreover, comparison of the different

395   tourmalines demonstrated that the *X* site is not responsible for tourmaline's extensive

396   (meta)stability.

397

398   As well as exerting a dominant control on tourmaline's compressibility and its unit-cell

399   parameters, the octahedral *Y* and *Z* sites show the largest degree of compositional variability. In

400   the tourmaline investigated here, these sites were solely occupied by Mg and Al, or in the case of

401   olenite, only Al. However, these sites can also be occupied by Li^+, Fe^{2+}, Fe^{3+}, Mn^{2+}, Cr^{3+}, V^{3+}, as

402   major constituents, or by Ni^{2+}, Co^{2+}, Cu^{2+}, Zn^{2+}, Ga^{3+}, Mn^{3+}, Ti^{4+} as minor constituents in natural

403   tourmaline (Bosi 2018). The varying size and charge of these ions, particularly those occurring at

404   the network-forming *Z* site, may have a minor effect on tourmaline's compressibility. A

405   significant povondraite [$NaFe^{3+}_3(Fe^{3+}_4Mg_2)Si_6O_{18}(BO_3)_3(OH)_3O$] component will significantly

406   expand tourmaline's unit-cell volume (**Fig. 2**) relative to Mg-Al tourmaline. It is therefore

407   expected that tourmaline with a large povondraite component may show increased

408   compressibility along **c** and correspondingly smaller K_0, an effect that would oppose the

409   stiffening effect of Al.

410

411   As the major host of B in the crust, the inclusion of tourmaline in geochemical models is vital to

412   developing an understanding of the B cycle. However, thermodynamic data for tourmaline is

413   lacking (van Hinsberg and Schumacher, 2007). The presented isothermal bulk moduli and their

414   pressure derivatives for synthetic tourmalines provide essential compressibility data for natural

415   Mg-Al tourmalines. These parameters are especially important for volume-sensitive reactions

416   common to environments of mass transfer. The results motivate the need for additional

417   compressibility studies on other near-end-member tourmalines, especially povondraite, as well as

418   the use of synthetic crystals in constraining other thermodynamic parameters, such as thermal

419   expansivities.

420

421   **Acknowledgements**

422

433

434   **References cited**

435   Angel, R.J. (2000) Equations of state. In: Hazen, R.M., Downs, R.T. (eds) High-temperature and

436   high-pressure crystal chemistry. Reviews in Mineralogy, 41, 35-60.

437

438   Angel, R.J., Gonzalez-Platas, J., and Alvaro, M. (2014) EosFit7c and a Fortran module (library)

439   for equation of state calculations. Zeitschrift für Kristallographie, 229, 405-419.

440

441   Armstrong, J.T. (1995) CITZAF: a package of correction programs for the quantitative electron

442   microbeam X-ray-analysis of thick polished materials, thin films, and particles. Microbeam

443   Analysis, 4, 177-200.

444

445   Bačík, P., Cempírek, J., Uher, P., Novák, M., Ozdín, D., Filip, J., Škoda, R., Breiter, K.,

446   Klementová, M., and Ďuďa, R. (2013) Oxy-schorl, $Na(Fe^{2+}_2Al)Al_6Si_6O_{18}(BO_3)_3(OH)_3O$, a new

447   mineral from Zlatá Idka, Slovak Republic and Přbyslavice, Czech Republic. American

448   Mineralogist, 98, 485–492.

449

450   Bačík, P., Ertl, A., Števko, M., Giester, G., and Sečkár, P. (2015) Acicular zoned tourmaline

451   (magnesio-foitite to foitite) from a quartz vein near Tisovec, Slovakia: the relationship between

452   crystal chemistry and acicular habit. Canadian Mineralogist, 53, 221–234.

453

454   Ballaran, T.B., Kurnosov, A., Glazyrin, K., Frost, D.J., Merlini, M., Hanfland, M., and Caracas,

455   R. (2012) Effect of chemistry on the compressibility of silicate perovskite in the lower mantle.

456   Earth and Planetary Science Letters, 333-334, 181-190.

457

458   Bass, J.D., Liebermann, R.C., Weidner, D.J., and Finch, S.J. (1981) Elastic properties from

459   acoustic and volume compression experiments. Physics of the Earth and Planetary Interiors, 25,

460   140-158.

461

462   Berryman, E., Wunder, B., and Rhede, D. (2014) Synthesis of K-dominant tourmaline. American

463   Mineralogist, 99, 539-542.

464

465   Berryman, E.J., Wunder, B., Wirth, R., Rhede, D., Schettler, G., Franz, G., and Heinrich, W.

466   (2015) An experimental study on K and Na incorporation in dravitic tourmaline and insight into

467   the origin of diamondiferous tourmaline from the Kokchetav Massif, Kazakhstan. Contributions

468   to Mineralogy and Petrology, 169, 28.

469

470   Berryman, E.J., Wunder, B., Rhede, D., Schettler, G., Franz, G., and Heinrich, W. (2016a) P-T-X

471   controls on Ca and Na distribution between Mg-Al tourmaline and fluid. Contributions to

472   Mineralogy and Petrology, 171, 31.

473

474   Berryman, E.J., Wunder, B., Ertl, A., Koch-Müller, M., Rhede, D., Scheidl, K., Giester, G., and

475   Heinrich, W. (2016b) Influence of the X-site composition on tourmaline's crystal structure:

476   investigation of synthetic K-dravite, dravite, oxy-uvite, and magnesio-foitite using SREF and

477   Raman spectroscopy. Physics and Chemistry of Minerals, 43, 83-102.

478

479   Bosi, F., and Lucchesi, S. (2007) Crystal chemical relationships in the tourmaline group:

480   structural constraints on chemical variability. American Mineralogist, 92, 1054–1063.

481

482   Bosi, F. (2008) Disordering of Fe^{2+} over octahedrally coordinated sites of tourmaline. American

483   Mineralogist, 93, 1647–1653.

484

485   Bosi, F. (2018) Tourmaline crystal chemistry. American Mineralogist, 103, 298-306.

486

487   Bosi, F., Balić- Žunić, T., and Surour, A.A. (2010) Crystal structure analyses of four tourmaline

488   specimens from the Cleopatra's Mines (Egypt) and Jabal Zalm (Saudi Arabia), and the role of Al

489   in the tourmaline group. American Mineralogist, 95, 510-518.

490

491   Bosi, F., Reznitskii, L., and Skogby, H. (2012) Oxy-chromium-dravite,

492    $NaCr_3(Cr_4Mg_2)(Si_6O_{18})(BO_3)_3(OH)_3O$, a new mineral species of the tourmaline supergroup.

493   American Mineralogist, 97, 2024–2030.

494

495   Bosi, F., Andreozzi, G.B., Skogby, H., Lussier, A.J., Abdu, Y., and Hawthorne, F.C. (2013a)

496   Fluor-elbaite, $Na(Li_{1.5}Al_{1.5})Al_6(Si_6O_{18})(BO_3)_3(OH)_3F$, a new mineral species of the tourmaline

497   supergroup. American Mineralogist, 98, 297–303.

498

499   Bosi, F., Reznitskii, L., and Sklyarov, E.V. (2013b) Oxy-vanadium-dravite,

500    $NaV_3(V_4Mg_2)(Si_6O_{18})(BO_3)_3(OH)_3O$: crystal structure and redefinition of the "vanadium-

501   dravite" tourmaline. American Mineralogist, 98, 501–505.

502   Bosi, F., Skogby, H., Hålenius, U., and Reznitskii, L. (2013c) Crystallographic and spectroscopic

503   characterization of Fe-bearing chromo-alumino-povondraite and its relations with oxy-

504   chromium-dravite and oxy-dravite. American Mineralogist, 98, 1557–1564.

505

506   Bosi, F., Reznitskii, L., Skogby, H., and Hålenius, U. (2014a) Vanadio-oxy-chromium- dravite,

507    $NaV_3(Cr_4Mg_2)(Si_6O_{18})(BO_3)_3(OH)_3O$, a new mineral species of the tourmaline supergroup.

508   American Mineralogist, 99, 1155–1162.

509

510   Bosi, F., Skogby, H., Reznitskii, L., and Hålenius, U. (2014b) Vanadio-oxy-dravite,

511    $NaV_3(Al_4Mg_2)(Si_6O_{18})(BO_3)_3(OH)_3O$, a new mineral species of the tourmaline supergroup.

512   American Mineralogist, 99, 218–224.

513

514   Bosi, F., Andreozzi, G.B., Hålenius, U., and Skogby, H. (2015a) Experimental evidence for

515   partial Fe^{2+} disorder at the Y and Z sites of tourmaline: a combined EMP, SREF, MS, IR and

516   OAS study of schorl. Mineralogical Magazine, 79, 515–528.

517

518   Bosi, F., Andreozzi, G.B., Agrosì, G., and Scandale, E. (2015b) Fluor-tsilaisite,

519    $NaMn_3Al_6(Si_6O_{18})(BO_3)_3(OH)_3F$, a new tourmaline from San Piero in Campo (Elba, Italy) and

520   new data on tsilaisitic tourmaline from the holotype specimen locality. Mineralogical Magazine,

521   79, 89–101.

522

523   Bosi, F., Skogby, H., Lazor, P., and Reznitskii, L. (2015c) Atomic arrangements around the O3

524   site in Al- and Cr-rich oxy-tourmalines: a combined EMP, SREF, FTIR and Raman study.

525   Physics and Chemistry of Minerals, 42, 441–453.

526

527   Bosi, F., Skogby, H., and Hålenius, U. (2016a) Thermally induced cation redistribution in Fe-

528   bearing oxy-dravite and potential geothermometric implications. Contributions to Mineralogy

529   and Petrology, 171, 47.

530

531   Bosi, F., Skogby, H., and Balić-Žunić, T. (2016b) Thermal stability of extended clusters in

532   dravite: a combined EMP, SREF and FTIR study. Physics and Chemistry of Minerals, 43, 395–

533   407.

534

535   Bosi, F., Reznitskii, L., Hålenius, U., and Skogby, H. (2017a) Crystal chemistry of Al-V-Cr oxy-

536   tourmalines from Sludyanka complex, Lake Baikal, Russia. European Journal of Mineralogy, 29,

537   457–472.

538

539   Bosi, F., Cámara, F., Ciriotti, M.E., Hålenius, U., Reznitskii, L., and Stagno, V. (2017b) Crystal-

540   chemical relations and classification problems of tourmalines belonging to the oxy-schorl–oxy-

541   dravite–bosiite–povondraite series. European Journal of Mineralogy, 29, 445–455.

542

543   Cempírek, J., Houzar, S., Novák, M., Groat, L.A., Selway, J.B., and Šrein, V. (2013) Crystal

544   structure and compositional evolution of vanadium-rich oxy-dravite from graphite quartzite at

545   Bítovánky, Czech Republic. Journal of Geosciencies, 58, 149–162.

546

547   Clark, C.M., Hawthorne, F.C., and Ottolini, L. (2011) Fluor-dravite,

548     $NaMg_3Al_6Si_6O_{18}(BO_3)_3(OH)_3F$, a new mineral species of the tourmaline group from the Crabtree

549   emerald mine, Mitchell County, North Carolina: description and crystal structure. Canadian

550   Mineralogist, 49, 57–62.

551

552   Clemens, P. and Prakapenka, V.B. (2015) DIOPTAS: a program for reduction of two-

553   dimensional X-ray diffraction data and data exploration. High Pressure Research, 35, 223-230.

554

555   Dera, P., Zhuravlev, K., Prakapenka, V., Rivers, M.L., Finkelstein, G.J., Grubor-Urosevic, O.,

556   Tschauner, O., Clark, S.M., and Downs, R.T. (2013) High pressure single-crystal micro X-ray

557   diffraction analysis with GSE_ADA/RSV software. High Pressure Research, 33, 466-484.

558

559   Dewaele, A., Loubeyre, P., and Mezouar, M. (2004) Equations of state of six metals above 94

560   GPa. Physical Review B, 70, 094112.

561

562   Dietrich R.V. (1985) The Tourmaline Group. Van Nostrand Reinhold Company, New York, 300

563   p.

564

565   Donnay, G. and Buerger, M.J. (1950) The determination of the crystal structure of tourmaline.

566   Acta Crystallographica A, 3, 379–388.

567

568   Ertl, A., Hughes, J.M., Prowatke, S., Rossman, G.R., London, D., and Fritz, E.A. (2003) Mn-rich

569   tourmaline from Austria: structure, chemistry, optical spectra, and relations to synthetic sold

570   solutions. American Mineralogist, 88, 1369-1376.

571

572   Ertl, A., Kolitsch, U., Prowatke, S., Dyar, M.D., and Henry, D.J. (2006) The F-analog of schorl

573   from Grasstein, Trentino–South Tyrol, Italy: crystal structure and chemistry. European Journal of

574   Mineralogy, 18, 583–588.

575

576   Ertl, A., Hughes, J.M., Prowatke, S., Ludwig, T., Brandstätter, F., Körner, W., and Dyar, M.D.

577   (2007) Tetrahedrally-coordinated boron in Li-bearing olenite from "mushroom" tourmaline from

578   Momeik, Myanmar: structure and chemistry. Canadian Mineralogist, 45, 891–899.

579

580   Ertl, A., Tillmanns, E., Ntaflos, C.F., Giester, G., Körner, W., Hughes, J.M., Lengauer, and C.,

581   Prem, M. (2008a) Tetrahedrally coordinated boron in Al-rich tourmaline and its relationship to

582   the pressure-temperature conditions of formation. European Journal of Mineralogy, 20, 881-888.

583

584   Ertl, A., Rossman, G.R., Hughes, J.M., Ma, C., and Brandstätter, F. (2008b) V^{3+}-bearing, Mg-

585   rich, strongly disordered olenite from a graphite deposit near Amstall, Lower Austria: A

586   structural, chemical and spectroscopic investigation. Neues Jahrbuch für Mineralogie

587   Abhandlungen, 184, 243–253.

588

589   Ertl, A., Kolitsch, U., Meyer, H.-P., Ludwig, T., Lengauer, C.L., Nasdala, L., and Tillmanns, E.

590   (2009) Substitution mechanism in tourmalines of the "fluor- elbaite"-rossmanite series from

591   Wolkenburg, Saxony, Germany. Neues Jahrbuch für Mineralogie Abhandlungen, 186, 51–61.

592

593   Ertl, A., Rossman, G.R., Hughes, J.M., London, D., Wang, Y., O'Leary, J.A., Dyar, M.D.,

594   Prowatke, S., Ludwig, T., and Tillmanns, E. (2010a) Tourmaline of the elbaite-schorl series from

595   the Himalaya Mine, Mesa Grande, California, U.S.A.: A detailed investigation. American

596   Mineralogist, 95, 24–40.

597

598   Ertl, A., Marschall, H.R., Giester, G., Henry, D.J., Schertl, H.-P., Ntaflos, T., Luvizotto, G.L.,

599   Nasdala, L., and Tillmanns, E. (2010b) Metamorphic ultra high-pressure tourmalines: Structure,

600   chemistry, and correlations to PT conditions. American Mineralogist, 95, 1–10.

601

602   Ertl, A., Mali, H., Schuster, R., Körner, W., Hughes, J.M., Brandstätter, F., and Tillmanns, E.

603   (2010c) Li-bearing, disordered Mg-rich tourmalines from the pegmatite-marble contact from the

604   Austroalpine basement units (Styria, Austria). Mineralogy and Petrology, 99, 89–104.

605

606   Ertl, A., Giester, G., Ludwig, T., Meyer, H.P., and Rossman, G.R. (2012a) Synthetic B-rich

607   olenite: Correlations of single-crystal structural data. American Mineralogist, 97, 1591-1597.

608

609   Ertl, A., Schuster, R., Hughes, J.M., Ludwig, T., Meyer, H.-P., Finger, F., Dyar, M.D., Ruschel,

610   K., Rossman, G.R., Klötzi, U., Brandstätter, F., Lengauer, C.L., and Tillmans, E. (2012b) Li-

611   bearing tourmalines in Variscan granitic pegmatites from the Moldanubian nappes, Lower

612   Austria. European Journal of Mineralogy, 24, 695–715.

613

614   Ertl, A., Kolitsch, U., Dyar, M.D., Hughes, J.M., Rossman, G.R., Pieczka, A., Henry, D.J.,

615   Pezzotta, F., Prowatke, S., Lengauer, C.L., Körner, W., Brandstätter, F., Francis, C.A., Prem, M.,

616   and Tillmanns, E. (2012c) Limitations of Fe^{2+}- and Mn^{2+}-rich and Mn^{2+} site occupancy in

617   tourmaline: evidence from Fe^{2+} tourmaline. American Mineralogist, 97, 1402–1416.

618

619   Ertl, A., Giester, G., Schüssler, U., Brätz, H., Okrusch, M., Tillmanns, E., and Bank, H. (2013)

620   Cu- and Mn-bearing tourmalines from Brazil and Mozambique: Crystal structures, chemistry and

621   Correlations. Mineralogy and Perology, 107, 265–279.

622

623   Ertl, A., Baksheev, I.A., Giester, G., Lengauer, C.L., Prokofiev, V.Y., and Zorina, L.D. (2016a)

624   Bosiite, $NaFe^{3+}_3(Al_4Mg_2)(Si_6O_{18})(BO_3)_3(OH)_3O$, a new ferric member of the tourmaline

625   supergroup from the Darasun gold deposit, Transbaikalia, Russia. European Journal of

626   Mineralogy, 28, 581–591.

627

628   Ertl, A., Kolitsch, U., Dyar, M.D., Meyer, H.-P., Henry, D.J., Rossman, G.R., Prem, M., Ludwig,

629   T., Nasdala, L., Lengauer, C.L., Tillmanns, E., and Niedermayr, G. (2016b) Fluor-schorl, a new

630   member of the tourmaline supergroup, and new data on schorl from the cotype localities.

631   European Journal of Mineralogy, 28, 163–177.

632

633   Ertl, A., Henry, D.J., Tillmanns, E. (2018) Tetrahedral substitutions in tourmaline: a review.

634   European Journal of Mineralogy, 30, 465-470.

635

636   Fan, D., Xu, J., Kuang, Y., Li, X., Li, Y., and Xie, H. (2015) Compressibility and equation of

637   state of beryl ($Be_3Al_2Si_6O_{18}$) by using a diamond anvil cell and in situ synchrotron X-ray

638   diffraction. Physics and Chemistry of Minerals, 42, 529-539.

639

640   Fei, Y., Ricolleau, A., Frank, M., Mibe, K., Shen, G., and Prakapenka, V. (2007) Toward an

641   internally consistent pressure scale. Proceedings of National Academy of Sciences, 104, 9182-

642   9186.

643

644   Filip, J., Bosi, F., Novák, M., Skogby, H., Tuček, J., Čuda, J., and Wildner, M. (2012) Redox

645   processes of iron in the tourmaline structure: Example of the high-temperature treatment of Fe^{3+}-

646   rich schorl. Geochimica et Cosmochimica Acta, 86, 239–256.

647

648   Finger, L.W., Hazen, R.M., Zou, G., Mao, H.K., and Bell, P.M. (1981) Structure and

649   compression of crystalline argon and neon at high pressure and room temperature. Applied

650   Physics Letters, 39, 892-894.

651

652   Finkelstein, G.J., Dera, P.K., and Duffy, T.S. (2015) High-pressure phases of cordierite from

653   single-crystal X-ray diffraction to 15 GPa. American Mineralogist, 100, 1821-1833.

654

655   Gatta, G.D., Danisi, R.M., Adamo, I., Meven, M., and Diella, V. (2012) A single- crystal neutron

656   and X-ray diffraction study of elbaite. Physics and Chemistry of Minerals, 39, 577–588.

657

658   Gonzalez-Platas, J., Alvaro, M., Nestola, F., and Angel, R. (2016) EosFit7-GUI: a new graphical

659   user interface for equation of state calculations, analyses and teaching. Journal of Applied

660   Crystallography, 49, 1377-1382.

661

662   Grew, E.S., Bosi, F., Gunter, M., Hålenius, U., Trumbull, R.B., and Yates, M.G. (2018) Fluor-

663   elbaite, lepidolite and Ta-Nb oxides from a pegmatite of the 3000 MA Sinceni pluton,

664   Swaziland: Evidence for lithium-cesium-tantalum (LCT) pegmatites in the Mesoarchean.

665   European Journal of Mineralogy, 30, 205-218.

666

667   Grice, J.D., Ercit, T.S., and Hawthorne, F.C. (1993) Povondraite, a redefinition of the tourmaline

668   ferridravite. American Mineralogist, 78, 433-436.

669

670   Hazen, R.M., Au, A.Y., and Finger, L.W. (1986) High-pressure crystal chemistry of beryl

671   ($Be_3Al_2Si_6O_{18}$) and euclase ($BeAlSiO_4OH$). American Mineralogist, 71, 977-984.

672

673   Helme, B.G. and King, P.J. (1978) The elastic constants of iron tourmaline (schörl). Journal of

674   Materials Science, 13, 1487-1489.

675

676   Hemingway, B.S., Evans, H.T., Jr., Mazdab, F.K., and Anovitz, L.M. (1996) Thermal expansion

677   of some borate and borosilicate minerals (fluoborite, danburite, sinhalite, datolite, elbaite,

678   dravite, kornerupine, dumortierite, ferro-axinite, and manganaxinite) between 25 and about

679   1200°C. US Geological Survey, Open File Report 96-100.

680

681   Henry, D.J. and Dutrow, B.L. (1992) Tourmaline in low grade clastic metasedimentary rock: an

682   example of the petrogenetic potential of tourmaline. Contributions to Mineralogy and Petrology,

683   112, 203-218.

684

685   Henry, D.J. and Dutrow, B.L. (1996) Metamorphic tourmaline. In: Grew, E.S., Anovitz, L.M.

686   (eds) Boron: mineralogy, petrology and geochemistry in the earth's crust. Reviews in

687   Mineralogy, 33, 500-555.

688

689   Henry, D.J. and Guidotti, C.V. (1985) Tourmaline as a petrogenetic indicator mineral: an

690   example from the staurolite-grade metapelites of NW Maine. American Mineralogist, 70, 1-15.

691

692   Henry, D.J., Novák, M., Hawthorne, F.C., Ertl, A., Dutrow, B.L., Uher, and P., Pezzotta, F.

693   (2011) Nomenclature of the tourmaline-supergroup minerals. American Mineralogist, 96, 895-

694   913.

695

696   Hughes, J.M., Ertl, A., Dyar, M.D., Grew, E.S., Shearer, C.K., Yates, M.G., and Guidotti, C.V.

697   (2000) Tetrahedrally coordinated boron in a tourmaline: boron-rich olenite from Stoffhütte,

698   Koralpe, Austria. The Canadian Mineralogist, 38, 861-868.

699

700   Hughes, K.-A., Hughes, J.M., and Dyar, M.D. (2001) Chemical and structural evidence for

701    $^{[4]}$B←→$^{[4]}$Si substitution in natural tourmalines. European Journal of Mineralogy, 13, 743-747.

702

703   Krosse, S. (1995) Hochdrucksynthese, Stabilität und Eigenschaften der Borsilikate Dravit und

704   Kornerupin sowie Darstellung und Stabilitätsverhalten eines neuen Mg–Al-borates. Dr. rer. nat.

705   thesis, Ruhr-Universität Bochum.

706

707   Kutzschbach, M., Wunder, B., Rhede, D., Koch-Müller, M., Ertl, A., Giester, G., and Heinrich,

708   W., Franz, G. (2016) Tetrahedral boron in natural and synthetic HP/UHP tourmaline: Evidence

709   from Raman spectroscopy, EMPA, and single-crystal XRD. American Mineralogist, 101, 93-

710   104.

711

712   Kutzschbach, M., Wunder, B., Trumbull, R.B., Rocholl, A., Meixner, A., and Heinrich, W.

713   (2017) An experimental approach to quantify the effect of tetrahedral boron in tourmaline on the

714   boron isotope fractionation between tourmaline and fluid. American Mineralogist, 102, 2505-

715   2511.

716

717   Larson, A.C. and von Dreele, R.B. (1987) Generalized structure analysis system. Los Alamos

718   National Laboratory Report LAUR 86-748.

719

720   Li, H., Qin, S., Zhu, X., Liu, J., Li, X., Wu, X., and Wu, Z. (2004) In situ high-pressure X-ray

721   diffraction of natural tourmaline. Nuclear Techniques, 27, 919-922. [In Chinese]

722

723   London, D., Ertl, A., Hughes, J.M., Morgan, G.B. VI, Fritz, E.A., and Harms, B.S. (2006)

724   Synthetic Ag-rich tourmaline: structure and chemistry. American Mineralogist, 91, 680-684.

725

726   Lussier, A.J., Aguiar, P.M., Michaelis, V.K., Kroeker, S., Herwig, S., Abdu, Y., and Hawthorne,

727   F.C. (2008) Mushroom elbaite from the Kat Chay mine, Momeik, near Mogok, Myanmar: I.

728   Crystal chemistry by SREF, EMPA, MAS NMR and Mössbauer spectroscopy. Mineralogical

729   Magazine, 72, 747–761.

730

731   Lussier, A.J., Hawthorne, F.C., Abdu, Y., Herwig, S., Michaelis, V.K., Aguiar, P.M., and

732   Kroeker, S. (2011a) The crystal chemistry of "wheatsheaf" tourmaline from Mogok, Myanmar.

733   Mineralogical Magazine, 72, 999–1010.

734

735   Lussier, A.J., Abdu, Y. Hawthorne, F.C., Michaelis, V.K., Aguiar, P.M., and Kroeker, S. (2011b)

736   Oscillatory zoned liddicoatite from Anjanabonoina, central Madagascar. I. Crystal chemistry and

737   structure by SREF and ^{11}B and ^{27}Al MAS NMR spectroscopy. Canadian Mineralogist, 49, 63–

738   88.

739

740   Lussier, A., Ball, N.A., Hawthorne, F.C., Henry, D.J., Shimizu, R., Ogasawara, Y., and Ota, T.

741   (2016) Maruyamaite, $K(MgAl_2)(Al_5Mg)Si_6O_{18}(BO_3)_3(OH)_3O$, a potassium-dominant tourmaline

742   from the ultrahigh-pressure Kokchetav massif, northern Kazakhstan: description and crystal

743   structure. American Mineralogist, 101, 355–361.

744

745   Marler, B., Borowski, M., Wodara, U., and Schreyer, W. (2002) Synthetic tourmaline (olenite)

746   with excess boron replacing silicon in the tetrahedral site: II. Structural analysis. European

747   Journal of Mineralogy, 14, 763-771.

748

749   Marschall, H.R., Ertl, A., Hughes, J.M., and McCommon, C. (2004) Metamorphic Na- and OH-

750   rich disordered dravite with tetrahedral boron associated with omphacite, from Syros, Greece:

751   Chemistry and structure. European Journal of Mineralogy, 16, 817-823.

752

753   Marschall, H.R., Korsakov, A.V., Luvizotto, G.L., Nasdala, L., and Ludwig, T. (2009) On the

754   occurrence and boron isotopic composition of tourmaline in (ultra)high-pressure metamorphic

755   rocks. Journal of the Geological Society, London, 166, 811-823.

756

757   Novák, M., Ertl, A., Povondra, P., Galiová, M.V., Rossman, G.R., Pristacz, H., Prem, M.,

758   Giester, G., Gadas, P., and Škoda, R. (2013) Darrellhenryite, $Na(LiAl_2)Al_6(BO_3)_3Si_6O_{18}(OH)_3O$,

759   a new mineral from the tourmaline supergroup. American Mineralogist, 98, 1886–1892.

760

761   O'Bannon, E., III, Beavers, C.M., Kunz, M., and Williams, Q. (2018) High-pressure study of

762   dravite tourmaline: Insights into the accommodating nature of the tourmaline structure.

763   American Mineralogist, 103, 1622-1633.

764

765   O'Bannon, E., III and Williams, Q. (2016) Beryl-II, a high-pressure phase of beryl: Raman and

766   luminescence spectroscopy to 16.4 GPa. Physics and Chemistry of Minerals, 43, 671-687.

767

768   Ogorodova, L.P., Melchakova, L.V., Kiseleva, I.A., and Peretyazhko, I.S. (2004)

769   Thermodynamics of natural tourmaline-elbaite. Thermochimica Acta, 419, 211-214.

770

771   Ota T., Kobayashi, K., Katsura, T., and Nakamura, E. (2008) Tourmaline breakdown in a pelitic

772   system: implications for boron cycling through subduction zones. Contributions to Mineralogy

773   and Petrology, 155, 19-32.

774

775   Pandey, C.S. and Schreuer, J. (2012) Elastic and piezoelectric constants of tourmaline single

776   crystals at non-ambient temperatures determined by resonant ultrasound spectroscopy. Journal of

777   Applied Physics, 111, 013516.

778

779   Plonka, A., Dera, P., Irmen, P., Rivers, M.L., Ehm, L., and Parise, J.B. (2012) β-diopside, a new

780   ultrahigh-pressure polymorph of $CaMgSi_2O_6$ with six-coordinated silicon. Geophysical Research

781   Letters, 39, L24307.

782

783   Prencipe, M., Scanavino, I., Nestola, F., Merlini, M., Civalleri, B., Bruno, and M., Dovesi, R.

784   (2011) High-pressure thermo-elastic properties of beryl ($Al_4Be_6Si_{12}O_{36}$) from ab initio

785   calculations, and observations about the source of thermal expansion. Physics and Chemistry of

786   Minerals, 38, 223-239.

787

788   Reznitskii, L., Clark, C.M., Hawthorne, F.C., Grice, J.D., Skogby, H., Hålenius, U., and Bosi, F.

789   (2014) Chromo-alumino-povondraite, $NaCr_3(Al_4Mg_2)(Si_6O_{18})(BO_3)_3(OH)_3O$, a new mineral

790   species of the tourmaline supergroup. American Mineralogist, 99, 1767–1773.

791

792   Rivers, M., Prakapenka, V.B., Kubo, A., Pullins, C., Holl, C.M., and Jacobsen, S.D. (2008) The

793   COMPRES/GSECARS gas-loading system for diamond anvil cells at the Advanced Photon

794   Source. High Pressure Research, 28, 273-292.

795

796   Schreyer, W., Wodara, U., Marler, B., van Aken, P., Seifert, F., and Robert, J.-L. (2000)

797   Synthetic tourmaline (olenite) with excess boron replacing silicon on the tetrahedral site: I.

798   Synthesis conditions, chemical and spectroscopic evidence. European Journal of Mineralogy, 12,

799   529-541.

800

801   Schreyer, W., Hughes, J.M., Bernhardt, H.-J., Kalt, A., Prowatke, S., and Ertl, A. (2002)

802   Reexamination of olenite from the type locality: Detection of boron in tetrahedral coordination.

803   European Journal of Mineralogy, 14, 935-942.

804

805   Setkova, T.V., Shapovalov, Y.B., and Balitskii, V.S. (2009) Experimental growth and structural-

806   morphological characteristics of Co-tourmaline. Doklady Earth Sciences, 424, 82-85.

807

808   Setkova, T.V., Balitsky, V.S., Vereschagin, O.S., and Shapovalov, Y.B. (2017) Hydrothermal

809   synthesis and morphology of Ga-bearing tourmaline. Doklady Earth Sciences, 473, 419-422.

810

811   Shimizu, R. and Ogasawara, Y. (2005) Discovery of K-tourmaline in diamond-bearing quartz-

812   rich rock from the Kokchetav Massif, Kazakhstan. Mitteilungen der Österreichischen

813   Mineralogischen Gesellschaft, 150, 141.

814

815   Singh, A.K. and Kenichi, T. (2001) Measurement and analysis of nonhydrostatic lattice strain

816   component in niobium to 145 GPa under various fluid pressure-transmitting media. Journal of

817   Applied Physics, 90, 3269-3275.

818

819   Tagg, S.L., Cho, H., Dyar, M.D., and Grew, E.S. (1999) Tetrahedral boron in naturally occurring

820   tourmaline. American Mineralogist, 84, 1451-1455.

821

822   Tatli, A. and Özkan, H. (1987) Variation of the elastic constants of tourmaline with chemical

823   composition. Physics and Chemistry of Minerals, 14, 172-176.

824

825   Tsuchiya, T. and Kawamura, K. (2002) Ab initio study of pressure effect on elastic properties of

826   crystalline Au. The Journal of Chemical Physics, 116, 2121-2124.

827

828   van Hinsberg, V.J. and Schumacher, J.C. (2007) Using estimated thermodynamic properties to

829   model accessory phases: the case of tourmaline. Journal of Metamorphic Geology, 25, 769-779.

830

831   van Hinsberg, V.J., Henry, D.J., and Marschall, H.R. (2011) Tourmaline: an ideal indicator of its

832   host environment. The Canadian Mineralogist, 49, 1-16.

833

834   von Goerne, G., Franz, G., and van Hinsberg, V.J. (2011) Experimental determination of Na-Ca

835   distribution between tourmaline and fluid in the system $CaO-Na_2O-MgO-Al_2O_3-SiO_2-B_2O_3-H_2O$.

836   The Canadian Mineralogist, 49, 137-152.

837

838   Welch, M.D., Cámara, F., Della Ventura, G., and Iezzi, G. (2007) Non-ambient in situ studies of

839   amphiboles. Reviews in Mineralogy and Geochemistry, 67, 223-260.

840

841   Wunder, B., Berryman, E., Plessen, B., Rhede, D., Koch-Müller, M., and Heinrich, W. (2015)

842   Synthetic and natural ammonium-bearing tourmaline. American Mineralogist, 100, 250-256.

843

844   Xia, X., Weidner, D.J., and Zhao, H. (1998) Equation of state of brucite: single-crystal Brillouin

845   spectroscopy study and polycrystalline pressure-volume-temperature measurement. American

846   Mineralogist, 83, 68-74.

847

848   Xu, J., Kuang, Y., Zhang, B., Liu, Y., Fan, D., Li, X., and Xie, H. (2016) Thermal equation of

849   state of natural tourmaline at high pressure and temperature. Physics and Chemistry of Minerals,

850   43, 315-326.

851

852   Xu, J., Zhang, D., Dawei, F., Dera, P., Shi, F., and Zhou, W. (2019) Thermoelastic properties of

853   eclogitic garnets and omphacites: implications for deep subduction of oceanic crust and density

854   anomalies in the upper mantle. Geophysical Research Letters, doi: 10.1029/2018GL081170

855

856   Yong, T., Dera, P., and Zhang, D. (2018) Single-crystal X-ray diffraction of grunerite up to 25.6

857   GPa: a high-pressure clinoamphibole polymorph. Physics and Chemistry of Minerals,

858   DOI:10.1007/s00269-018-0999-1

859

860   Zhang, L. (1998) Single crystal hydrostatic compression of $(Mg, Mn, Fe, Co)_2SiO_4$ olivines.

861   Physics and Chemistry of Minerals, 25, 308-312.

862

863   Zhang, L., Ahsbahs, H., Kutoglu, A., and Geiger, C.A. (1999) Single-crystal hydrostatic

864   compression of synthetic pyrope, almandine, spessartine, grossular and andradite garnets at high

865   pressures. Physics and Chemistry of Minerals, 27, 52-58.

866

867 **Table 1. Tourmaline Equation of State Parameters**

Synthetic Tourmaline	K_0 (GPa)	K_0'	V_0 (Å^3)	K_0 (GPa)	K_0'	V_0 (Å^3)	
Dravite	97(6)	5.0(5)	1556(4)	110(2)	[4]	1551(3)	This study
K-dravite	109(4)	4.3(2)	1567(3)	115(1)	[4]	1564(2)	
Oxy-uvite	110(2)	4.1(1)	1573(2)	112.5(6)	[4]	1571(1)	
Magnesio-foitite	116(2)	3.5(1)	1560(2)	105.8(9)	[4]	1568(2)	
Olenite	116(6)	4.7(4)	1490(4)	128(2)	[4]	1485(3)	
Natural tourmaline							
Dravite	110(3)	4.6(8)	1578.2(2)	112(1)	[4]	1578.2(2)	O'Bannon et al. (2018)
Uvite	97(1)	12.4(4)	1537(1)	120(2)	[4]	1537(1)	Xu et al. (2012)
Elbaite-schorl	119[a]		1542				Pandy and Schreuer (2012)
Elbaite-schorl	118[a]		1542				
Elbaite-schorl	117[a]		1568				
Schorl-dravite	116[a]		1578				
Schorl-dravite	118[a]		1578				
Schorl	120[a]		1553				Tatli and Özkan (1987)
Elbaite	115[a]		1555				
Elbaite	114[a]		1545				
Elbaite	115[a]		1542				
Uvite	115[a]		1586				
Schorl-elbaite	121[a]		1550				Helme and King (1978)

868 [a] Isothermal bulk moduli calculated from isentropic bulk moduli using the volume thermal expansivity of
869 Pandy and Schreuer (2012) and the constant-pressure specific heat of Ogorodova et al. (2004).
870 Brackets indicate the value was fixed during fitting.

871 **Table 2. Investigated synthetic tourmalines general cation site occupancies $[XY_3Z_6T_6O_{18}(BO_3)_3V_3W]$**

	$^{[9]}X$	$^{[6]}Y$	$^{[6]}Z$	$^{[4]}T$
Dravite[a]	0.84(6) **Na**, 0.16(6) •	1.8(6) **Mg**, 1.2(7) Al	5.3(6) **Al**, 0.7(6) Mg	5.6(3) **Si**, 0.1(4) Al, 0.4(2) B
K-dravite[a]	0.5(1) **K**, 0.5(1) • , 0.1(5) Na	1.8(6) **Mg**, 1.3(6) Al	5.4(5) **Al**, 0.6(5) Mg	5.7(2) **Si**, 0.2(2) Al, 0.2(1) B
Oxy-uvite	0.64(1) **Ca**, 0.36(1) •	1.5(1) **Mg**, 1.5(1) **Al**	4.9(2) **Al**, 1.1(2) Mg	6 **Si**
Magnesio-foitite	0.91(6) • , 0.09(6) Na	1.4(2) **Mg**, 1.6(2) **Al**	4.9(2) **Al**, 1.1(2) Mg	5.66(4) **Si**, 0.34(4) B
Olenite	0.58(1) **Na**, 0.42(1) •	2.83(1) **Al**	6 **Al**	4.6(1) **Si**, 1.4(1) B

872 • indicates vacancy. Brackets indicate coordination number of site. Bold typeface indicates major site-occupying ion.
873 Values for oxy-uvite (sample CN11) and magnesio-foitite (sample MF2) are from Berryman et al. (2016b). Values for olenite (sample MK1,
874 columnar) from Kutzschbach et al. (2016). These studies determined the site occupancies by a combination of EMPA and structure refinement of
875 single-crystal XRD diffraction data.
876 [a]Site occupancies determined by normalization of EMPA to 18 cations at the Y, Z, and T sites. Mg-Al disorder between Y and Z sites calculated
877 using empirical relationship of Bosi(2018). See supplementary material for additional details.
878

879

Table 3. High-pressure unit cell parameters

Dravite

Pressure (GPa)	a (Å)	c (Å)	V (Å^3)
0.76(4)	15.806(3)	7.163(2)	1549.8(6)
2.72(4)	15.743(3)	7.043(2)	1511.7(5)
4.83(5)	15.672(3)	6.986(2)	1485.9(6)
8.41(5)	15.584(3)	6.881(2)	1447.3(7)
12.66(5)	15.476(3)	6.772(2)	1404.6(5)
17.61(5)	15.373(3)	6.688(2)	1368.7(5)
21.80(6)	15.289(4)	6.619(2)	1340.0(7)
26.24(6)	15.199(4)	6.553(2)	1311.1(7)
30.48(6)	15.115(3)	6.479(2)	1281.9(6)
33.57(6)	15.067(3)	6.452(2)	1268.4(6)
36.08(7)	15.014(3)	6.417(2)	1252.7(4)

880

K-dravite

Pressure (GPa)	a (Å)	c (Å)	V (Å^3)
1.24(4)	15.857(3)	7.145(1)	1556.0(4)
2.68(4)	15.818(2)	7.060(1)	1529.8(4)
4.71(5)	15.753(3)	6.990(1)	1502.3(5)
7.36(5)	15.687(2)	6.919(1)	1474.5(3)
11.89(5)	15.580(1)	6.807(1)	1430.8(3)
15.71(5)	15.491(3)	6.731(1)	1398.7(5)
19.67(6)	15.399(2)	6.666(1)	1369.0(4)
33.68(7)	15.149(4)	6.475(2)	1286.7(5)
24.10(6)	15.297(2)	6.606(1)	1338.7(4)
28.00(6)	15.253(2)	6.548(1)	1319.4(3)
30.70(6)	15.199(4)	6.506(1)	1301.7(5)
36.26(7)	15.096(4)	6.443(1)	1271.5(5)
38.66(7)	15.053(4)	6.414(1)	1258.6(5)
41.08(7)	15.005(3)	6.393(1)	1246.6(5)
43.57(7)	14.960(4)	6.358(2)	1232.3(6)
45.96(7)	14.934(3)	6.345(1)	1225.4(5)
48.26(8)	14.888(4)	6.323(1)	1213.7(5)
50.57(8)	14.847(4)	6.308(1)	1204.1(5)

881

Oxy-uvite

Pressure (GPa)	a (Å)	c (Å)	V (Å^3)
1.85(4)	15.862(1)	7.1118(3)	1549.7(1)
3.73(5)	15.783(2)	7.0543(4)	1521.8(2)

5.76(5)	15.733(3)	6.9974(9)	1499.9(5)
7.80(5)	15.703(1)	6.9247(3)	1478.8(2)
10.58(5)	15.624(3)	6.8521(8)	1448.6(5)
16.44(5)	15.488(3)	6.7214(8)	1396.4(5)
18.56(6)	15.452(4)	6.682(1)	1381.6(5)
20.85(6)	15.398(3)	6.6455(8)	1364.5(4)
23.21(6)	15.350(3)	6.6067(8)	1348.1(4)
25.82(6)	15.306(3)	6.5704(8)	1333.0(4)
27.51(6)	15.267(3)	6.5433(8)	1320.7(4)
29.53(6)	15.227(3)	6.5162(9)	1308.3(4)
31.67(6)	15.196(1)	6.4895(6)	1297.7(2)
33.69(7)	15.157(3)	6.4636(9)	1285.9(4)
35.65(7)	15.118(2)	6.4379(5)	1274.3(2)
38.12(7)	15.076(3)	6.4145(8)	1262.6(4)
40.23(7)	15.045(2)	6.3856(5)	1251.8(3)
43.04(7)	15.013(2)	6.3634(6)	1242.0(3)
45.55(7)	14.960(4)	6.334(1)	1228.1(5)
48.40(8)	14.915(3)	6.3095(5)	1215.5(4)
51.62(8)	14.863(4)	6.2833(6)	1202.1(4)
52.72(8)	14.859(2)	6.2745(6)	1199.8(3)
53.92(8)	14.837(2)	6.2636(5)	1194.1(3)
55.06(8)	14.802(4)	6.249(1)	1185.6(5)
57.30(8)	14.755(5)	6.229(1)	1174.5(6)

882

Magnesio-foitite

Pressure (GPa)	a (Å)	c (Å)	V (Å^3)
1.08(4)	15.869(2)	7.091(1)	1546.5(4)
1.86(4)	15.843(2)	7.064(1)	1535.5(4)
5.63(5)	15.742(2)	6.941(1)	1489.6(3)
8.16(5)	15.681(3)	6.883(1)	1465.6(5)
10.61(5)	15.614(2)	6.825(1)	1441.0(3)
13.44(5)	15.544(3)	6.764(1)	1415.4(4)
16.92(5)	15.473(2)	6.703(1)	1389.9(3)
18.69(6)	15.417(1)	6.661(1)	1371.2(2)
20.34(6)	15.388(1)	6.641(1)	1361.9(3)
21.81(6)	15.348(1)	6.612(1)	1348.8(2)
24.38(6)	15.284(3)	6.580(2)	1331.1(4)
26.91(6)	15.233(1)	6.539(1)	1314.1(3)
29.55(6)	15.145(4)	6.493(2)	1289.9(6)
31.54(6)	15.129(1)	6.476(1)	1283.5(2)

34.19(7)	15.088(2)	6.436(1)	1268.8(3)
36.25(7)	15.038(1)	6.424(1)	1258.1(2)
38.99(7)	14.992(3)	6.395(1)	1244.7(4)
40.93(7)	14.959(3)	6.374(1)	1235.1(4)
43.08(7)	14.921(3)	6.346(1)	1223.6(4)
44.78(7)	14.887(3)	6.334(1)	1215.7(4)
46.76(7)	14.848(2)	6.317(1)	1206.1(3)
48.90(8)	14.836(3)	6.300(1)	1201.0(4)
49.80(8)	14.813(1)	6.290(1)	1195.2(2)
51.66(8)	14.789(2)	6.274(1)	1188.2(3)
54.04(8)	14.738(3)	6.248(1)	1175.2(5)
56.00(8)	14.702(3)	6.236(1)	1167.3(4)
56.94(8)	14.681(2)	6.228(1)	1162.5(3)
58.00(8)	14.640(3)	6.222(1)	1154.9(4)
58.94(8)	14.638(2)	6.216(1)	1153.6(3)

883

Olenite

Pressure (GPa)	a (Å)	c (Å)	V (Å³)
1.18(4)	15.610(5)	7.001(2)	1477.3(8)
2.72(4)	15.559(5)	6.938(2)	1454.5(8)
6.78(5)	15.458(5)	6.840(3)	1415.4(9)
9.63(5)	15.398(6)	6.773(3)	1390.9(9)
13.27(5)	15.307(3)	6.719(2)	1363.2(6)
17.68(5)	15.226(4)	6.615(2)	1328.0(7)
21.48(6)	15.142(4)	6.546(2)	1299.9(7)
25.91(6)	15.066(3)	6.479(2)	1273.5(6)
30.27(6)	14.995(3)	6.424(2)	1250.8(5)
33.36(6)	14.947(3)	6.410(2)	1239.2(6)
35.87(7)	14.914(3)	6.384(2)	1229.8(5)
38.20(7)	14.878(3)	6.372(1)	1221.4(4)
40.68(7)	14.819(3)	6.314(1)	1200.8(4)
43.45(7)	14.802(4)	6.290(2)	1193.6(6)
45.41(7)	14.766(4)	6.286(2)	1187.0(6)
47.42(7)	14.735(4)	6.263(2)	1177.6(6)
49.41(8)	14.723(4)	6.246(2)	1172.6(5)
51.40(8)	14.699(4)	6.226(2)	1165.0(6)

884

885   **Table 4. Tourmaline axial compressibility**

Synthetic Tourmaline	β_{a0} (10^{-3} GPa^{-1})	M_{a0} (GPa)	M_{a0}'	a_0 (Å)	β_{c0} (10^{-3} GPa^{-1})	M_{c0} (GPa)	M_{c0}'	c_0 (Å)	
Dravite	1.98(6)	505(16)	12(1)	15.824(5)	7.1(6)	141(13)	14(1)	7.185(13)	This study
K-dravite	1.83(5)	547(16)	9.7(7)	15.889(6)	6.4(3)	156(8)	14.0(6)	7.181(9)	
Oxy-uvite	1.82(4)	551(13)	9.9(6)	15.907(5)	6.6(2)	151(4)	13.1(2)	7.204(5)	
Magnesio-foitite	1.88(4)	532(12)	8.0(4)	15.907(5)	5.6(1)	179(4)	12.4(2)	7.134(5)	
Olenite	1.83(7)	546(20)	13(1)	15.639(8)	5.1(5)	195(18)	12(1)	7.040(16)	
Natural tourmaline									
Dravite[a]	2.09(5)	480(11)	16(2)	15.937	5.0(1)	201(4)	10.0(9)	7.1749	O'Bannon et al. (2018)
Uvite[a]	2.4(2)	424(25)	33(8)	15.823(6)	5.4(3)	185(8)	31(4)	7.089(4)	Xu et al. (2012)

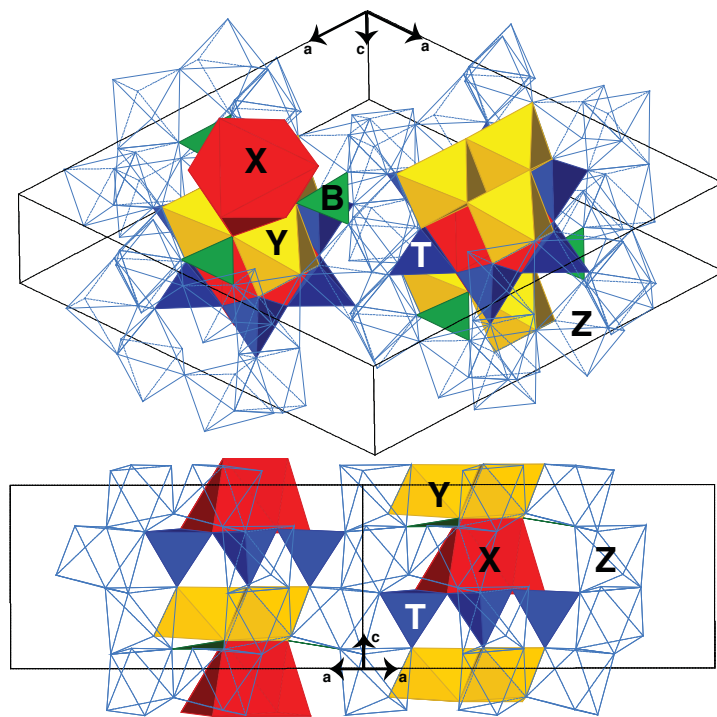886   [a]Fit done using the data presented in these studies.
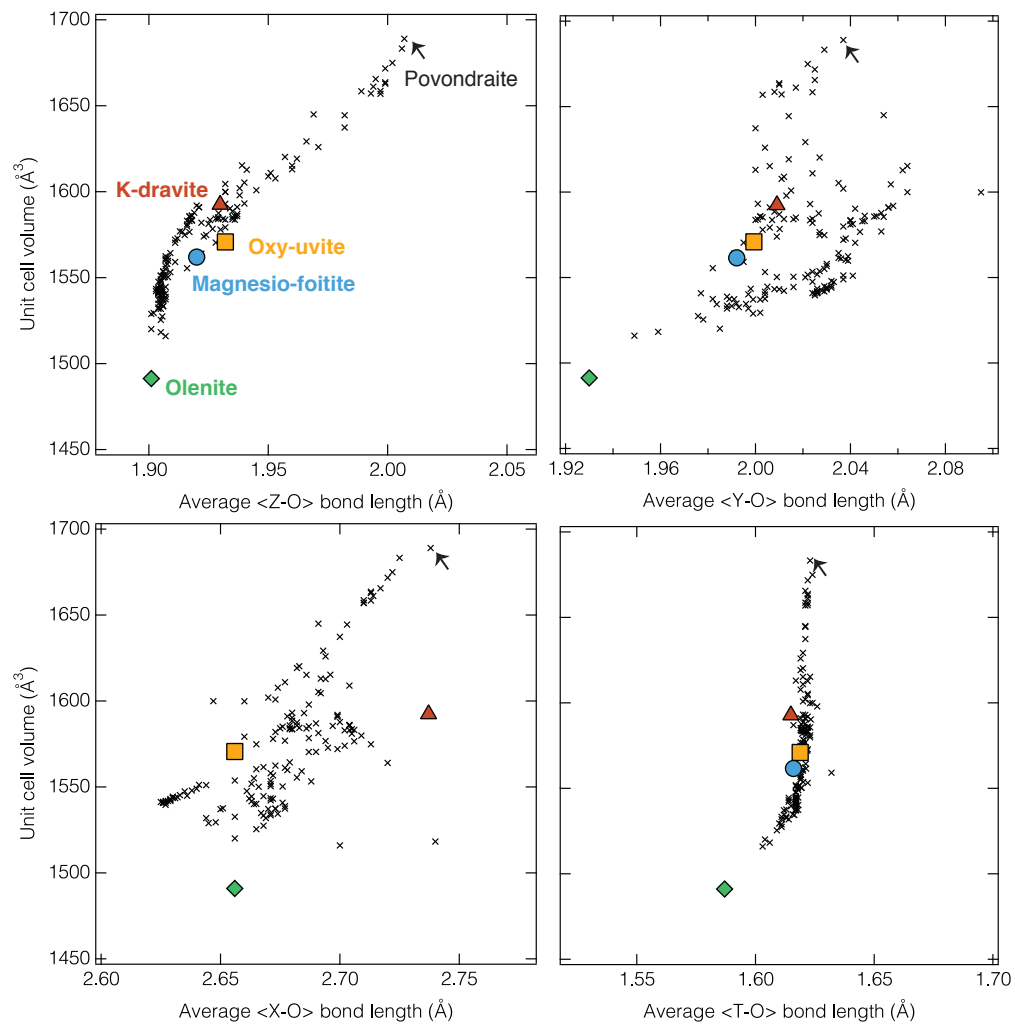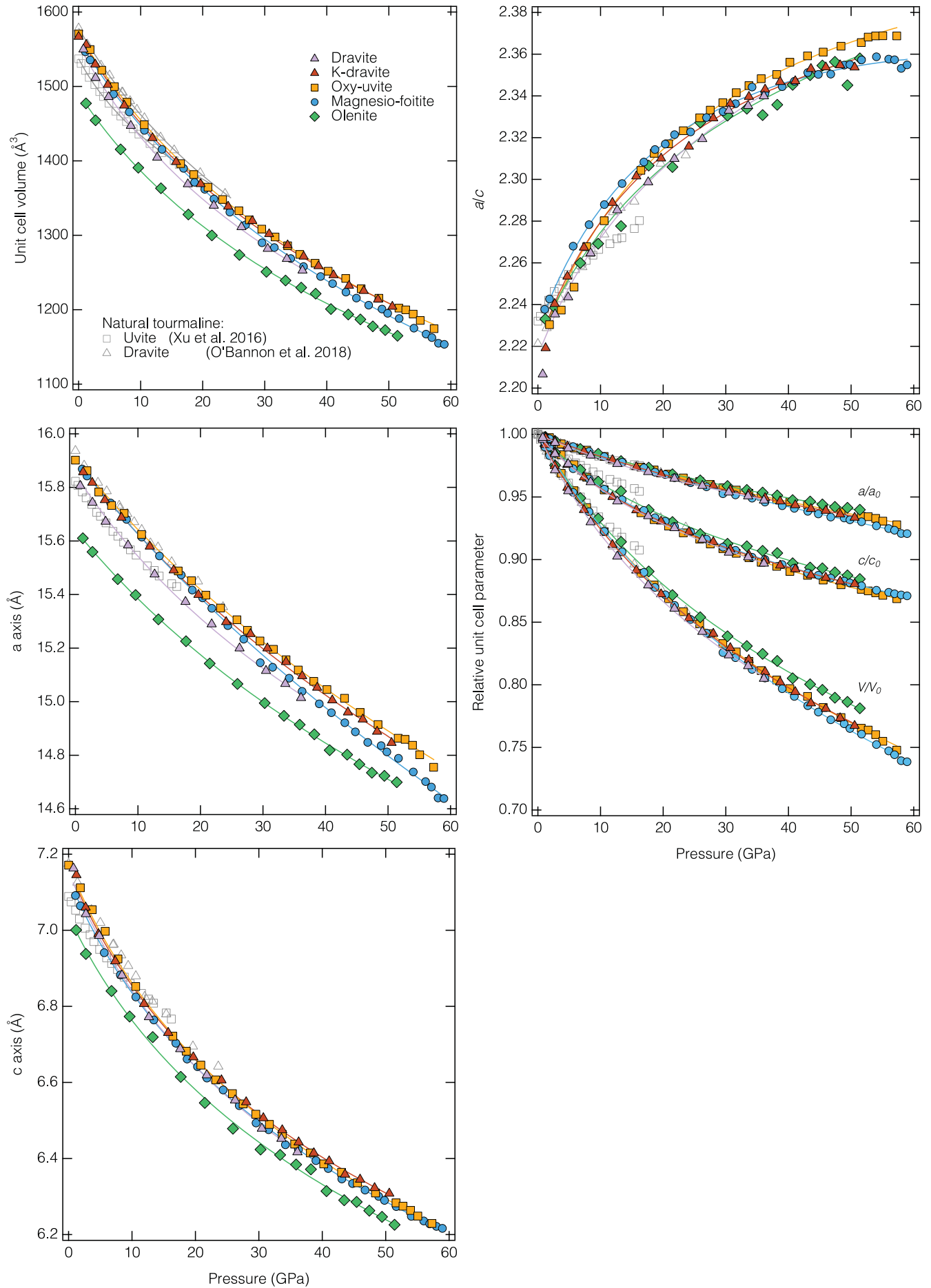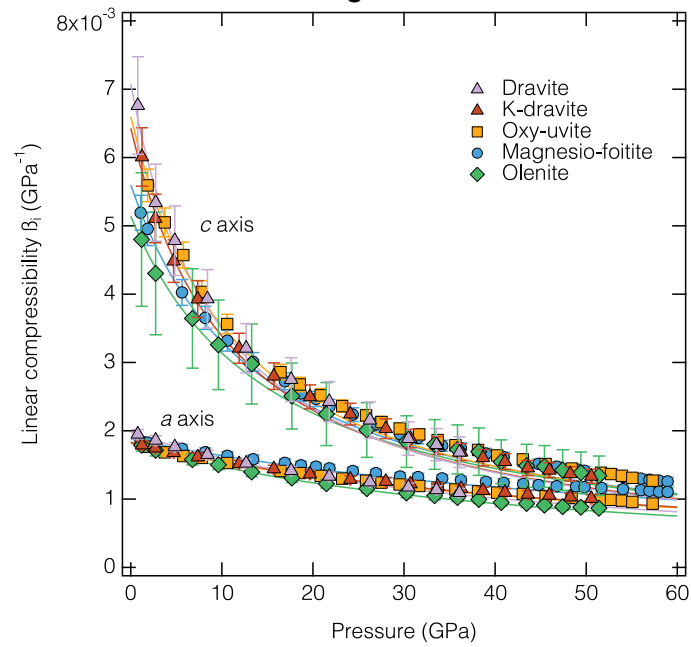
887

45

Fig. 1 $XY_3Z_6T_6O_{18}(BO_3)_3V_3W$

Fig. 2

Fig. 3

Fig. 4

Fig. 5

Fig. 6